Compact and wideband transmit opto-antenna for radio frequency over fiber

OLIVIER CAYTAN[1,*], LAURENS BOGAERT[1,2], HAOLIN LI[1], JORIS VAN KERREBROUCK[1], SAM LEMEY[1], SAM AGNEESSENS[1], JOHAN BAUWELINCK[1], PIET DEMEESTER[1], GUY TORFS[1], DRIES VANDE GINSTE[1], AND HENDRIK ROGIER[1]

[1] *Electromagnetics Group, IDLab, Department of Information Technology, Ghent University/imec, 9000 Ghent, Belgium*
[2] *Photonics Research Group, Department of Information Technology, Ghent University/imec, 9000 Ghent, Belgium*
[*] *Olivier.Caytan@UGent.be*

Abstract: An advanced transmit remote opto-antenna unit is proposed that accomplishes impedance matching between a photodetector and a low profile antenna in a specified frequency bandwidth, without requiring an area-consuming matching network. This results in a highly compact design, which also avoids the losses and spurious radiation by such an electrically large matching circuit. Instead, the photodetector is almost directly connected to the antenna, which is designed as a conjugate load, such that the extracted and radiated power are optimized. The required input impedance for the antenna is obtained by adopting a half-mode air-filled substrate-integrated-waveguide topology, which also exhibits excellent radiation efficiency. The proposed unit omits electrical amplifiers and is, therefore, completely driven by the signal supplied by an optical fiber when deployed in an analog optical link, except for an externally supplied photodetector bias voltage. Such a highly cost-effective, power-efficient and reliable unit is an important step in making innovative wireless communication systems, which deploy extremely dense attocells of 15 cm × 15 cm, technically and economically feasible. As a validation, a prototype, operating in the Unlicensed National Information Infrastructure radio bands (5.15 GHz–5.85 GHz), is constructed and its radiation properties are characterized in free-space conditions. After normalizing with respect to the optical source's slope efficiency, a maximum boresight gain of 12.0 dBi and a −3 dB gain bandwidth of 1020 MHz (18.6 %) are observed.

1. Introduction

Radio over fiber (RoF) architectures exhibit great potential for realizing next-generation wireless communication systems [1, 2]. They rely on the favorable properties of fiber-optic signal propagation, most notably high bandwidth and low propagation loss, for the exchange of radio signals between a central office (CO) and multiple remote antenna units (RAUs). Hardware for routing, switching and processing of the radio signals is centralized at the CO and can be shared to reduce cost, while also greatly decreasing the complexity of the RAU hardware. This is especially pronounced in the case of analog radio frequency over fiber (RFoF) schemes [1], where the radio-frequency (RF) signals are immediately modulated onto the optical carrier and the RAUs only need to implement conversion between the optical and electrical domains. Owing to the heavily reduced cost and complexity per RAU, RFoF architectures are prime candidates to implement systems requiring extreme cell densification.

This letter focuses on a novel, compact transmit RAU for application in the downlink (DL) subsystem of the ultra-high density wireless communication system introduced in [3, 4]. This novel, highly specialized communication system targets a futuristic factory that is densely

populated by numerous autonomous robots. Each robot requires high-bandwidth, time-critical and reliable wireless access to high-performance computing resources. To realize the resulting density of extremely high-bit-rate mobile users, a massive amount of optically-fed RAUs are integrated into the factory floor, operating in attocells as small as 15 cm × 15 cm. Finally, the foreseen operation at millimeter-wave (mm-wave) frequencies guarantees the availability of sufficient bandwidth, and helps to reduce interference between adjacent cells. The development of low-cost and low-power RAUs is necessary to make this massive deployment cost-effective.

To this end, this letter proposes a novel compact transmit RAU with minimal complexity and cost. By omitting electrical amplifiers, which is justifiable when considering the low propagation distances in the intended application [3], an extremely reliable design is obtained that only consists of a photodetector interconnected with an antenna. The proposed low-profile unit is, therefore, nearly passive and almost entirely driven by optical power, only requiring electrical DC power to bias the photodetector. Specifically, this letter investigates the design of a wideband transmit RAU with optimal power efficiency, within these constraints. This is achieved by tuning the input impedance of the antenna to an optimal frequency-dependent impedance, rather than a fixed 50 Ω impedance, such that as much RF power as possible is extracted from the output port of the photodetector and radiated by the antenna, within a wide specified frequency band. As a proof of principle, we construct and validate a prototype that operates from 5.15 GHz to 5.85 GHz, covering several Unlicensed National Information Infrastructure (U-NII) radio bands [5].

Several transmit RAUs that omit electrical amplifiers have already been proposed in literature, including designs based on horn antennas [6, 7], patch antennas [8–10], slot antennas [11], planar log-periodic toothed antennas [12], and tightly coupled arrays [13–16]. However, none of them focus on optimizing the input impedance of the antenna such that it extracts as much power as possible from the photodetector within a specified frequency range. Wideband operation allows employing the transmit antenna for multiple functionalities [13], but, unfortunately, results in a suboptimal RoF link gain [17], as a consequence of the Fano-Bode limit [18, 19]. In contrast, [20] proposes a fully passive transmit RAU that accomplishes impedance matching between a low profile antenna and a zero-biased photodetector in a specified frequency bandwidth. To this end, a mixed lumped/distributed impedance matching network transforms the antenna's radiation impedance, designed to be 50 Ω, to match with the photodetector's impedance in the frequency band of interest. In contrast to [20], the design proposed in this letter achieves impedance matching by tuning the antenna impedance itself, instead of relying on an external matching network, thereby eliminating all distributed elements. This results in a much more compact design, while eliminating all losses and spurious radiation associated to the radial stubs employed in the external impedance matching network of [20].

As in [20], the antenna is based on air-filled substrate-integrated-waveguide (AFSIW) technology [21], which is essentially a planar implementation of the conventional air-filled rectangular metallic waveguide inside a multi-layer printed circuit board (PCB). This is realized by milling out a cavity in a low-cost single-substrate dual-layer PCB. This cavity implements the air-filled region of the rectangular waveguide structure. To contain the electromagnetic fields, the inner sidewalls are subsequently metalized through edge-plating, such that the fields cannot penetrate the dielectric substrate. The final AFSIW structure is obtained by covering the milled substrate on both sides with additional conductive layers. Electrical contact between the different layers, as well as mechanical strength, is ensured by means of soldering [21] or tightening alignment pins [22]. Through wideband transitions, the resulting AFSIW can be interfaced to microstrip lines [21], or other AFSIWs [23]. Several AFSIW components have already been reported, including filters [21] and antennas [22]. These retain the compelling advantages of conventional air-filled metallic waveguide components, including low loss, high quality factor, and excellent electrical shielding between components, while remaining compatible with standard PCB fabrication processes.

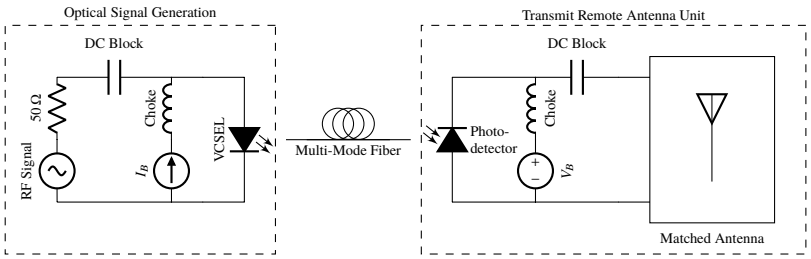

Fig. 1. High-level functional overview of the proposed transmit remote antenna unit.

In Section 2, the design process of the proposed transmit RAU is outlined, providing details about the adopted RFoF scheme, the impedance matching technique, the antenna topology, and the optimization of the entire structure. Subsequently, Section 3 presents the radiation pattern measurements conducted on a prototype of the proposed unit. Finally, in Section 4, a conclusion is formulated, and an outlook for further research is provided.

2. Design aspects of the transmit remote antenna unit

2.1. Overview

Figure 1 provides a functional overview of the proposed transmit RAU. On a high level, the design consists of a photodetector that is interconnected to an antenna with a conjugate-matched input impedance. The photodetector is reversely biased by a voltage source V_B through a bias tee, represented by an ideal choke and an ideal coupling capacitor. A multi-mode fiber illuminates the active region of the photodetector, which acts as the receiver in an intensity modulation and direct detection (IM-DD) scheme. A vertical-cavity surface-emitting laser (VCSEL), biased by a current I_B, is employed as an optical source. An RF signal, whose power is contained within the frequency band ranging from 5.15 GHz to 5.85 GHz, directly modulates the VCSEL, such that an optical double sideband (ODSB) signal is launched into the fiber. The adoption of a VCSEL with a direct modulation scheme and multi-mode fiber enhances cost effectiveness, such that massive deployment of the proposed transmit RAU in the wireless communication system proposed in [3] is facilitated. Nevertheless, the proposed conjugate-impedance matching technique can be applied without any modification to photodetectors operating at longer wavelengths using single-mode fiber and externally modulated optical sources. For now, the fiber link is assumed to be sufficiently short, such that the fiber's propagation loss and dispersion can be neglected. The antenna's input impedance is conjugate-matched, such that as much RF power as possible is extracted from the photodetector within this frequency bandwidth, and subsequently radiated. This is in contrast to [20], where the antenna was designed to exhibit a 50 Ω input impedance, while an external matching network, containing area-consuming distributed elements, transformed the antenna's impedance to achieve matching with the photodetector's output impedance. By eliminating these distributed elements, a more compact and more efficient design is obtained, in the meantime reducing spurious radiation.

As electrical amplifiers are omitted, the power radiated by the RAU originates entirely from the high-frequency component of the photocurrent, generated in response to the ODSB signal illuminating the photodetector. Conjugate-impedance matching between the photodetector and antenna is ensured to optimize the RF power extracted from the photodetector and radiated by the antenna. This results in a power-efficient unit with reduced complexity and cost that is passive, apart from requiring an externally supplied photodetector bias voltage. Additionally, if the increased nonlinear response of the photodetector can be tolerated [24], the photodetector can be operated at zero-bias, such that a fully passive transmit RAU is obtained [20]. Although electrical

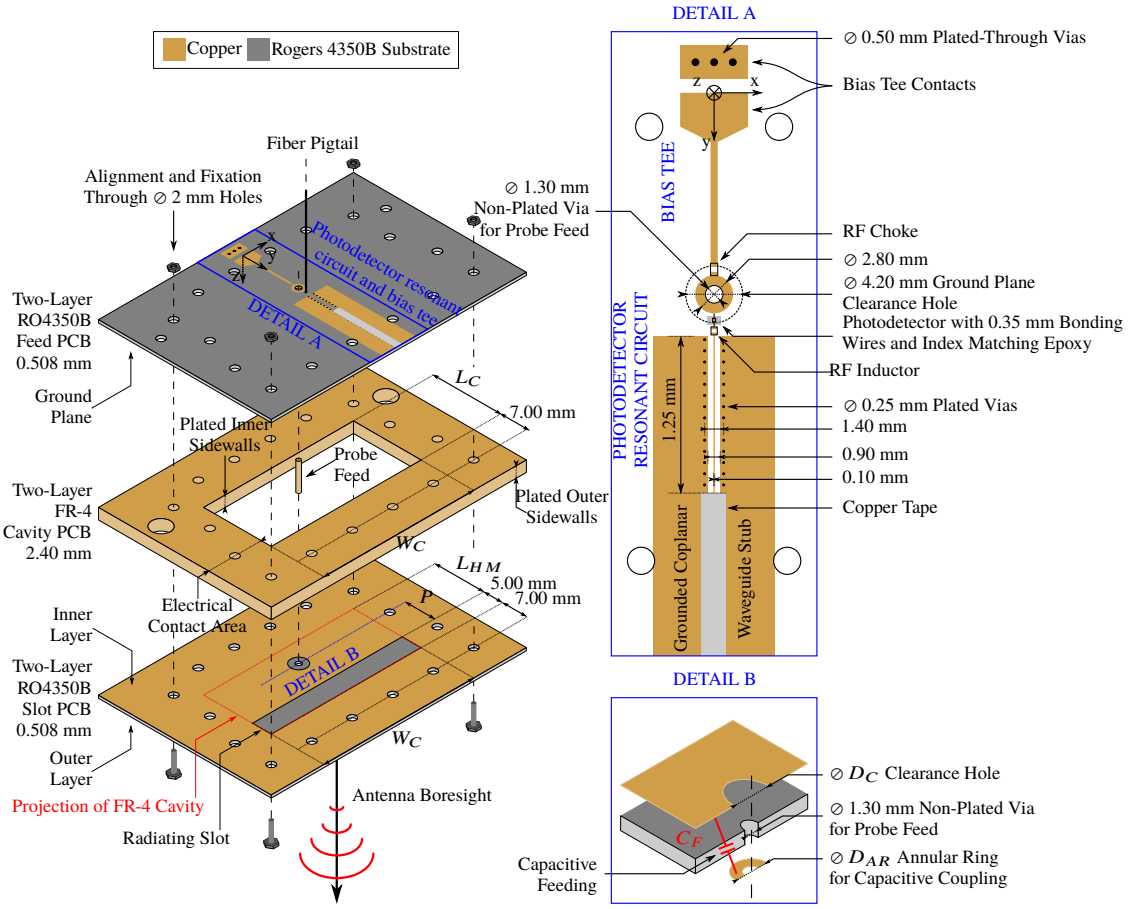

Fig. 2. Exploded view of the proposed transmit remote antenna unit. Initial and optimized values of the design parameters are provided in Table 1. Detail A focuses on the feed PCB which contains the photodetector resonant circuit and the bias tee, while detail B focuses on the antenna's capacitive feeding mechanism.

amplifiers are omitted, the radiated power can be increased by increasing the power of the RF signal modulating the VCSEL. Nevertheless, care must be taken that the nonlinear distortion introduced by the VCSEL [25, 26] and photodetector remains limited to avoid degradation of the link performance. This ultimately restricts the radiated power and useful communication range of the unit. Owing to its low complexity and cost, as well as its high reliability, the proposed transmit RAU is ideal for massive deployment in the ultra-high density communication system introduced in [3]. The limited radiated power is acceptable when considering that the units are deployed in attocells as small as 15 cm × 15 cm, resulting in extremely short wireless propagation distances.

Figure 2 presents an exploded view of the proposed transmit RAU, and shows in detail the three constituent single-substrate dual-layer PCBs, being the feed PCB, the cavity PCB, and the slot PCB. The feed PCB is implemented on a Rogers 4350B high-frequency laminate ($\epsilon_r = 3.66$, $\tan\delta = 0.0023$). The feed structure is responsible for providing the photodetector with a bias voltage and a short interconnection towards the matched AFSIW antenna. This matched AFSIW antenna structure consists of the slot PCB, also implemented on a Rogers 4350B high-frequency laminate, along with the FR-4 ($\epsilon_r \approx 4.08$, $\tan\delta \approx 0.013$) cavity PCB, which implements the

milled and edge-plated cavity filled with air. The matched antenna structure is excited by a probe feed that interconnects the outer conducting layers of the feed and slot PCBs. Each PCB also contains an identical set of non-plated vias, which are used for accurate alignment and tightening of all three PCBs in a stack, by routing M2 nylon screws through them. This also guarantees a good electrical contact between the touching conducting layers of two stacked PCBs.

2.2. Conjugate impedance matching of the photodetector

To achieve conjugate matching between the antenna and the photodetector, accurate knowledge of the output impedance of the latter is essential. The employed photodetector is a commercial 25 Gbps PIN photodiode by Albis Optoelectronics (PDCS32T-GS), which is optimized for a wavelength around 850 nm with a nominal responsivity of $0.53\,\mathrm{A\,W^{-1}}$. This device is quite compact ($350\,\mu\mathrm{m} \times 300\,\mu\mathrm{m}$, with a thickness of $150\,\mu\mathrm{m}$), and exposes two contacts, being the cathode and anode, as well as the active region on the same side. To enable top illumination of the active region, both contacts are wire bonded to the feed PCB. The small-signal output impedance has been characterized in dark conditions at several reverse bias voltages, by means of a Keysight N5242A PNA-X vector network analyzer (VNA) and a calibrated Picoprobe 40A-GS-125-DP microwave probe. The measured output impedance only slightly changes when increasing the reverse bias voltage from 0 V to 5 V. Specifically, a value of 1 V is chosen. The impedance measured at this bias voltage, shown in Fig. 3(a), is fitted to the equivalent circuit model, shown in Fig. 3(b), which consists of a parallel connection of a photocurrent source i_p, a junction capacitance C_P, and a resistance R_P, in series with a resistance R_S [27]. It was found that the resistor R_P is very large and can be omitted. Analytically, the internal impedance Z_{PD} of the photodetector is therefore given by

$$Z_{PD}(s) = R_S + \frac{1}{sC_P}, \tag{1}$$

with $s = j\omega$, and ω the angular frequency expressed in radians per second. In order to extract maximum power from such a generator, it should be loaded by the conjugate of its internal impedance Z_{PD}^* [28]. This maximum available power is then given by

$$P_{AV} = \frac{1}{8} \cdot \frac{|i_p|^2}{\omega^2 C_P^2 R_S}. \tag{2}$$

When the photodetector is loaded by a different impedance, the power P_L delivered to this impedance will only be a fraction of the maximum available power P_{AV}. This fraction is defined as the transducer gain $G_T = P_L/P_{AV}$ [28].

The challenge and novelty of the current design consists in devising an antenna structure with an input impedance that approximates a conjugate load over the ultra-wide bandwidth (5.15 GHz – 5.85 GHz), which is not trivial. The proposed approach starts by identifying an appropriate antenna input impedance $Z_A(j\omega)$ for this purpose. This is achieved by proceeding as if a band pass Chebyshev impedance matching network is synthesized for the photodetector's equivalent circuit, being a resistor/capacitor series combination, according to the procedure outlined in [29, 30]. Such a lossless matching network maximizes the minimum transducer gain within the specified frequency band [29]. As shown in Fig. 4(a), the procedure adds an inductor L_S in series to the photodetector. This series inductor L_S and the photodetector together form a series RLC circuit, which resonates at 5.49 GHz, being the geometrical center of the frequency band of interest (5.15 GHz – 5.85 GHz). In what follows, this resonator is referred to as the photodetector resonant circuit. The series inductor L_S is realized by a chip inductor and the bonding wires, and entails electrical parasitics that slightly transform the photodetector's small-signal impedance, which is modeled by a very low resistance R_S and capacitance C_P. As a

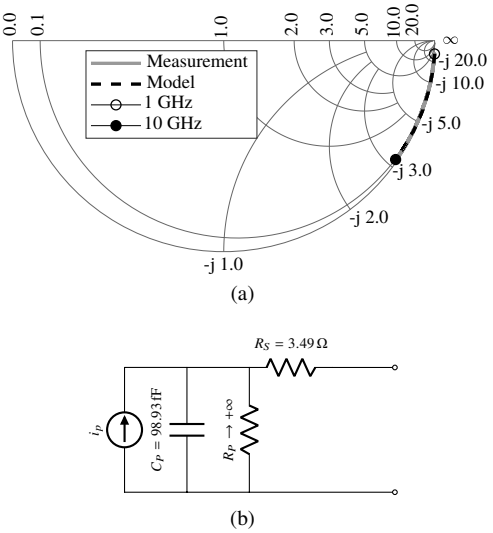

Fig. 3. (a) Measurement of the photodiode's small-signal impedance at a reverse bias voltage of 1 V in dark conditions. (b) Photodetector small-signal equivalent circuit model for a bias voltage of 1 V.

different photodetector impedance gives rise to a matching network with different element values, it is important to consider the design and implementation of the photodetector resonant circuit first. An accurate full-wave simulation model of the photodetector resonant circuit, including the bonding wires and a model for the chip inductor, will produce an accurate estimation of its output impedance $Z_{OUT}(j\omega)$, which is subsequently used to synthesize the full matching network. All full-wave simulations, presented in this letter, are performed using the frequency solver of CST Microwave Studio 2018.

The photodetector resonant circuit is implemented on the feed PCB and is shown in detail in Fig. 2. In addition, the feed PCB also contains an RF choke and two contacts, which are used to bias the photodetector. A functional overview of the photodetector resonant circuit is provided in Fig. 4(a), which summarizes the different contributions to the required series inductance L_S. First of all, the photodetector is connected to the feed PCB by two short aluminum bonding wires with a diameter of 18 µm, bridging a distance of 350 µm. By placing the photodetector inside a small cavity, milled in the substrate, its upper surface is level with that of the PCB, such that very short bonding wires can be applied. As a result, the parasitic resistance of the bonding wires is limited, as well as their contribution to the total required series inductance L_S, such that variations in bonding wire profile only influence performance in a minor degree. An important contribution to L_S is delivered by a 3.4 nH chip inductor. Additionally, a grounded coplanar waveguide (GCPW) stub is added. The stub is terminated by a short at a variable position by applying copper tape. The input impedance of the stub is therefore given by $Z_{GCPW} = jZ_c \tan(kl)$, with Z_c the characteristic impedance of the stub, k the wave number and l the stub length. Hence, the stub can be employed as a variable inductance, provided its electrical length is kept sufficiently short. The optimal length was found to be 1.25 mm during full-wave simulation, such that approximately 0.75 nH of inductance can be removed by tuning the stub length. Although part of the antenna feed structure, a final contribution L_F to the total series inductance L_S is delivered by the feeding probe that connects the photodetector resonant circuit to the AFSIW antenna through a 1.30 mm non-plated via. To prevent shorting the probe, a clearance hole (Fig. 2, detail A) with a diameter of 4.20 mm is present in the feed PCB's ground plane, which is, for the rest, entirely uninterrupted. The AFSIW antenna employs a capacitive feeding scheme, explained in detail

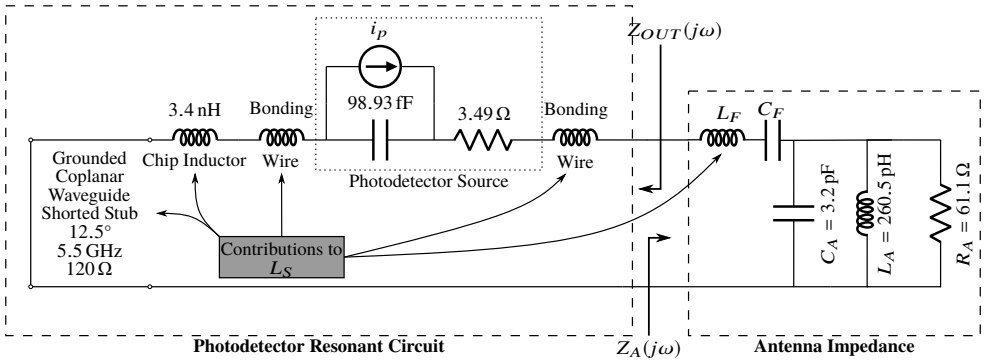

(a)

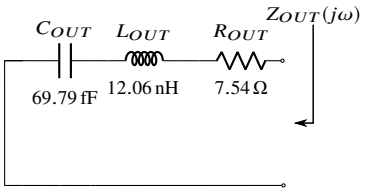

(b)

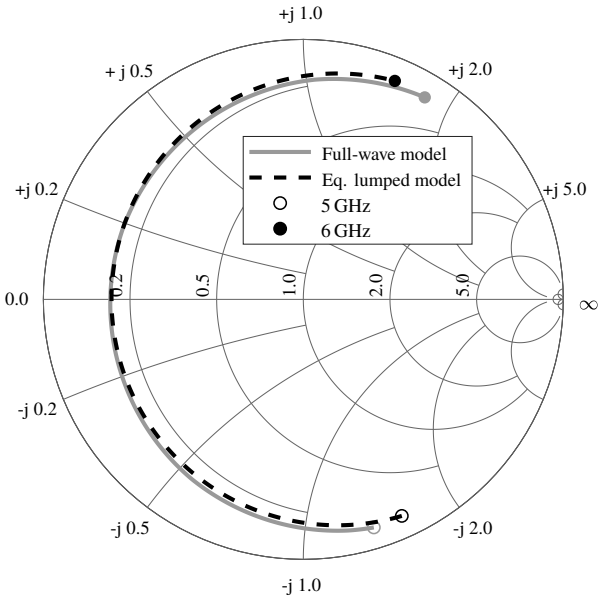

(c)

Fig. 4. (a) Synthesis of a second-order Chebyshev matching network to determine the required antenna input impedance. (b) Lumped circuit model for the output impedance $Z_{OUT}(j\omega)$ of the photodetector resonant circuit. (c) Comparison of the output impedance of the photodetector resonant circuit obtained with the full-wave simulation and the lumped circuit model.

in Subsection 2.3, that allows to compensate the reactance added by the feeding probe. This is indicated by the capacitor C_F in Fig. 4(a).

Subsequently, to enable application of the analytical procedure outlined in [29, 30], the output impedance $Z_{OUT}(j\omega)$ of the photodetector resonant circuit obtained by full-wave simulation, as indicated in Fig. 4(a), is fitted to a lumped series RLC resonator. The resulting equivalent circuit is shown in Fig. 4(b). The values of the capacitor C_{OUT} and resistor R_{OUT} are slightly changed compared to the ones of the equivalent circuit of the photodetector at a bias voltage of 1 V, shown in Fig. 3(b). Several effects, including parasitics related to the soldering pads, parasitic resistance of the chip inductor and wire bonds, caused by the skin effect, as well as small transmission line effects arising from an implementation with realistically spaced components, slightly change the values of the resistance and reactance slope of the resonator. Despite this, an excellent agreement between the lumped model and the full-wave simulation model for $Z_{OUT}(j\omega)$ is obtained, as proven by Fig. 4(c).

Finally, using the generator impedance shown in Fig. 4(b), a second-order Chebyshev impedance matching network is synthesized for the frequency band ranging from 5.1 GHz to 5.9 GHz, covering the frequency band of interest with slight margins. As shown in Fig. 4(a), this results in a parallel LC resonator ($C_A \parallel L_A$), resonating at the geometrical center of the frequency band of interest, and a resistive load R_A. While in [20], R_A was considered to be the antenna with a frequency-independent resistive input impedance, and the shunt LC resonator was realized as a shunt radial stub, here, the entire parallel RLC resonator ($C_A \parallel L_A \parallel R_A$) is considered to be the input impedance of an appropriately designed antenna, instead. This results in an extremely compact matching network, that only consists of the shorted GCPW stub, a chip inductor, and the two bonding wires, as shown in detail A of Fig. 2.

2.3. Matched air-filled half-mode substrate-integrated-waveguide antenna

The half-mode cavity-backed slot antenna structure with conjugate-matched input impedance is formed by the ground plane of the feed PCB, the cavity PCB and the slot PCB, as shown in Fig. 2. A rectangular cavity of dimensions $L_C \times W_C$ is milled in the cavity PCB, such that the medium containing the cavity fields is air. The cavity's inner sidewalls are metalized, such that the fields do not penetrate the lossy FR-4 substrate. For the same reason, the outer sidewalls of the entire PCB containing the cavity are also edge-plated, as indicated in Fig. 2. The ground plane of the feed PCB and the slot PCB cover this milled cavity, and form an $L_{HM} \times W_C$ rectangular half-mode substrate-integrated-waveguide resonator, as discussed in [31, 32]. Essentially, such a half-mode AFSIW resonator is a miniaturization of the conventional rectangular waveguide cavity [28]. By bisecting the rectangular waveguide cavity along one of its symmetry planes, which also acts as a quasi-magnetic wall, only half of the original structure is retained, while its modal field distribution and resonance frequency are only slightly disturbed [31, 32]. The resonator shown in Fig. 2 is designed to support a half TE_{110} mode at a resonance frequency of 5.49 GHz. Besides miniaturization, the bisection also results in radiation emanating from the open edge, and the structure operates as an antenna. To allow the radiation to escape from the half-mode AFSIW resonator, a 5.0 mm $\times W_C$ slot is also etched in the inner layer. The structure is excited by a capacitive feeding mechanism [33], which is shown in detail B in Fig. 2. Electrical contact between the probe and the slot PCB's inner conducting layer is avoided by a clearance hole with a diameter D_C. Instead, the probe is soldered to an annular ring on the slot PCB's outer layer. The overlap between the outer and inner conducting layers of the slot PCB forms a capacitor, which is able to support the high-frequency current applied by the probe feed. As shown in detail B of Fig. 2, the annular ring diameter D_{AR} and the clearance hole diameter D_C allow tuning the structure's capacitance. Therefore, they serve as additional degrees of freedom during the optimization of the antenna structure. Furthermore, with this feeding mechanism, the antenna structure itself incorporates the decoupling capacitor (DC block) present in Fig. 1, which

is essential for correct operation of the bias tee.

Similar to microstrip patch antennas [34], it was found that the input impedance of the proposed half-mode AFSIW cavity could be effectively modeled near its resonance frequency as a parallel RLC resonator [28], when adopting a series inductor as a very basic model for the probe feeding mechanism. A parallel RLC resonator is uniquely defined by its resistance value R, inductance value L, and capacitance value C, or equivalently, by its resonance frequency, given by

$$f_r = \frac{1}{2\pi\sqrt{LC}}, \tag{3}$$

by its quality factor, given by

$$Q = R\sqrt{\frac{C}{L}}, \tag{4}$$

and by its resistance at resonance, R. The parallel RLC resonator that achieves impedance matching with the photodetector resonant circuit, which is shown in Fig. 4(a), has a resonance frequency of 5.49 GHz, a resistance at resonance of 61.1 Ω, and a very low quality factor of 6.8. As the AFSIW resonator is designed to support a half TE_{110} mode, the resonance frequency is immediately controlled by adjusting the cavity dimensions [31, 32]. Furthermore, the resonance resistance is controlled by adjusting the probe offset P, which is indicated in Fig. 2. Owing to the air substrate, which is almost lossless and exhibits a very low dielectric constant, practically equal to 1, and the fairly large substrate thickness of 2.40 mm, the proposed AFSIW resonator can achieve very low quality factors around the required value of 6.8, which was impossible to achieve by means of dielectric-filled cavities. Additional adjustment of the resonator's quality factor is obtained by tuning the cavity width W_C, while keeping the resonance frequency f_r constant by controlling the cavity length L_{HM}, and keeping the resonance resistance constant by controlling the probe offset P. Figure 5 shows the resulting quality factor, and the required cavity length L_{HM} and probe offset P, for different values of the cavity width W_C, while keeping the resonance frequency constant at 5.49 GHz and the resonance resistance constant at 61.1 Ω. These design curves were generated by means of several full-wave simulations, assuming that the excitation probe makes direct contact with the slot PCB's inner layer. It was also found that the slot length $L_C - L_{HM}$ has a slight influence on the obtained quality factor, but this dimension was fixed at 5.00 mm, in order to secure accurate fabrication. Figure 5 is used to obtain the initial dimensions of the matched AFSIW antenna, which are summarized in the second column of Table 1. Finally, Fig. 6(b) proves that the input impedance of the initially dimensioned half-mode AFSIW cavity, obtained by full-wave simulation, is accurately modeled by the equivalent circuit model shown in Fig. 6(a). The capacitance C_F, which models the capacitor formed by the overlap between the outer and inner conducting layers of the slot PCB (Fig. 2, detail B), approaches infinity as the excitation probe makes direct contact with the slot PCB's inner layer. By optimizing the parameters that control this capacitive feeding, being the annular ring diameter D_{AR} and the clearance hole diameter D_C, the capacitance C_F becomes finite, and the probe inductance L_F can be counteracted.

Full-wave simulations predict excellent radiation properties, which remain stable over the entire frequency band of interest (5.15 GHz – 5.85 GHz). The antenna's radiation is linearly polarized, with the YZ-plane being the E-plane, which contains the far-field electric field vector, and the XZ-plane being the H-plane, which contains the far-field magnetic field vector. The simulated far-field gain patterns in these E- and H-planes, at the lower frequency 5.15 GHz, center frequency 5.50 GHz, and at the upper frequency 5.85 GHz, are shown in Fig. 7 by the black solid lines. All patterns are normalized with respect to the maximum value. The antenna exhibits a directional radiation pattern with a single lobe in the frontal hemisphere ($z > 0$). The direction of maximum gain is contained in the YZ-plane ($\phi = 90°$), and is slightly tilted with respect to the z-axis ($\theta = 18°$), which is explained by the single radiating edge of the antenna. Nevertheless,

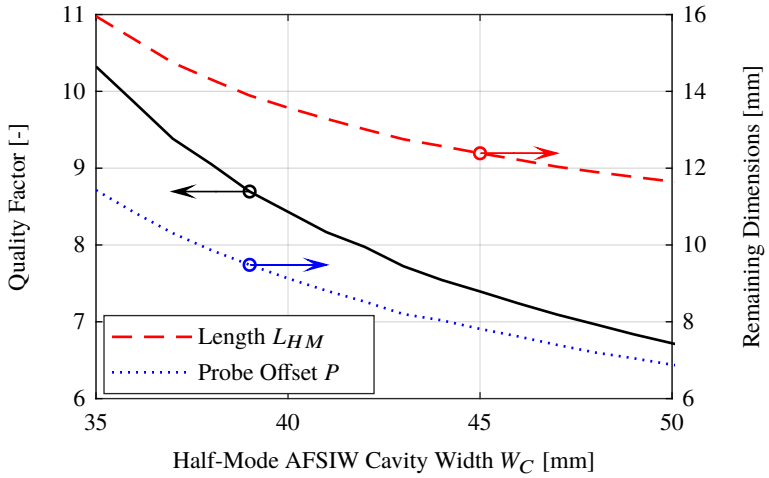

Fig. 5. Design curves for tuning the quality factor Q of the proposed air-filled half-mode substrate-integrated-waveguide antenna, while preserving a resonance frequency of 5.49 GHz and a resonance resistance of 61.1 Ω.

Table 1. Transmit remote antenna unit dimensions, before and after optimization.

Dimension [mm]	Optimized	Preliminary
W_C	39.79	48.00
L_{HM}	12.95	11.90
P	7.62	7.20
D_C	3.08	0.00
D_{AR}	2.72	2.80

over the entire frequency band of interest, the main lobe direction shifts by no more than 4° in the YZ-plane. For convenience, the $+z$ direction is defined as the antenna boresight. The far-field gain at 5.50 GHz equals 7.06 dBi, and remains very stable, changing only by 0.36 dB over the considered frequency interval. Furthermore, in the frontal hemisphere, the cross-polarization level is below −30 dB in the E-plane, and below −17 dB in the H-plane. Finally, the simulated radiation efficiency amounts to over 98 %, owing to the use of the air cavity, which is practically lossless.

2.4. Full-wave optimization of the transmit remote antenna unit

After the initial design of the constituent parts, being the photodetector resonant circuit and the matched AFSIW antenna, the performance of the entire transmit RAU is optimized by full-wave simulation. The number of design parameters is limited, as shown in Table 1, and their starting values are already close to optimal, such that full-wave optimization of a combined model is feasible. A final optimization step is necessary, because the values for the annular ring diameter D_{AR} and the clearance hole diameter D_C of the capacitive feeding that counteracts the probe inductance L_F, have not yet been determined. Apart from being crucial for the conjugate matching of the photodetector and the antenna, the capacitive coupling is also exploited to implement the

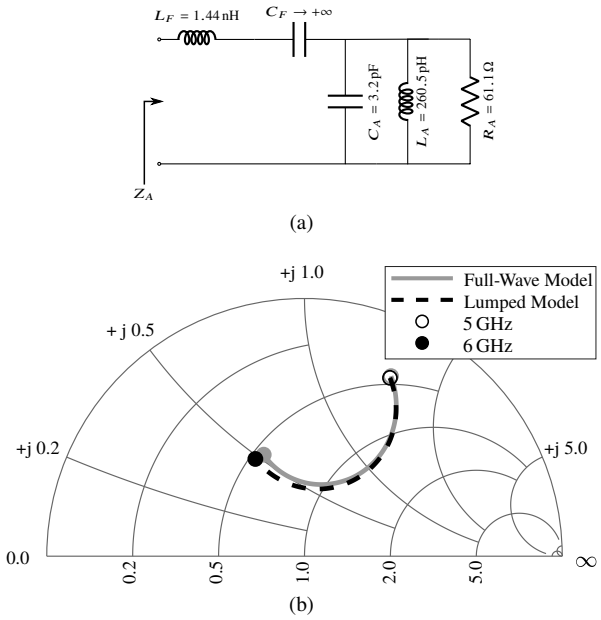

Fig. 6. (a) Equivalent circuit model for the input impedance of the half-mode air-filled substrate-integrated-waveguide (AFSIW) antenna. (b) Comparison of the input impedance of the half-mode AFSIW antenna obtained with the full-wave simulation and with the equivalent circuit model.

DC blocking of the bias tee. The remaining bias tee functionality is realized by a 15.0 nH chip inductor, which serves as an RF choke. This component is also added to the simulation model. Finally, the index-matching epoxy, which is deposited on the photodetector to attach the fiber pigtail, is also taken into account in the full-wave simulation model. As the epoxy sits around the bonding wires, it has an important influence on the impedance matching. To achieve accurate alignment, the pigtail is excited by an 850 nm optical source, while positioning its cleaved end near the active region of the photodetector where the photocurrent is maximal. Subsequently, the cleaved end is glued to this location, by means of an ultra-violet (UV) light-cured epoxy (EPO-TEK OG142-112). The glue is modeled by a 1.0 mm × 0.6 mm × 0.1 mm rectangular cuboid, centered at the photodetector. Its dielectric constant is estimated to be 3. The presence of the glue clearly influences the resonance frequency of the photodetector resonant circuit, with a change in the glue's dielectric constant of ±2 resulting in a resonance frequency shift of ±120 MHz.

From a practical point of view, the most interesting figure of merit for the proposed transmit RAU is the far-field boresight gain, with the reference plane at the modulation input of the optical source, as shown in Fig. 8. A problematic consequence of this approach is that the performance of the transmit RAU would depend on the properties of the optical source and the optical interconnection. Yet, in the simulation model, this can be circumvented by adopting an ideal optical source, with an input impedance of 50 Ω and a slope efficiency of 1 W A^{-1}, and assuming a lossless optical back-to-back connection between the optical source and transmit RAU. Using the simulation setup and with respect to the reference plane shown in Fig. 8, the far-field boresight gain of the transmit RAU is optimized in the frequency band of interest (5.15 GHz – 5.85 GHz), resulting in the optimized dimensions listed in the first column of Table 1. The corresponding optimized far-field boresight gain is shown by the black solid line in Fig. 9. The gain remains stable within 3 dB in the frequency band ranging from 5.07 GHz to 5.91 GHz (being

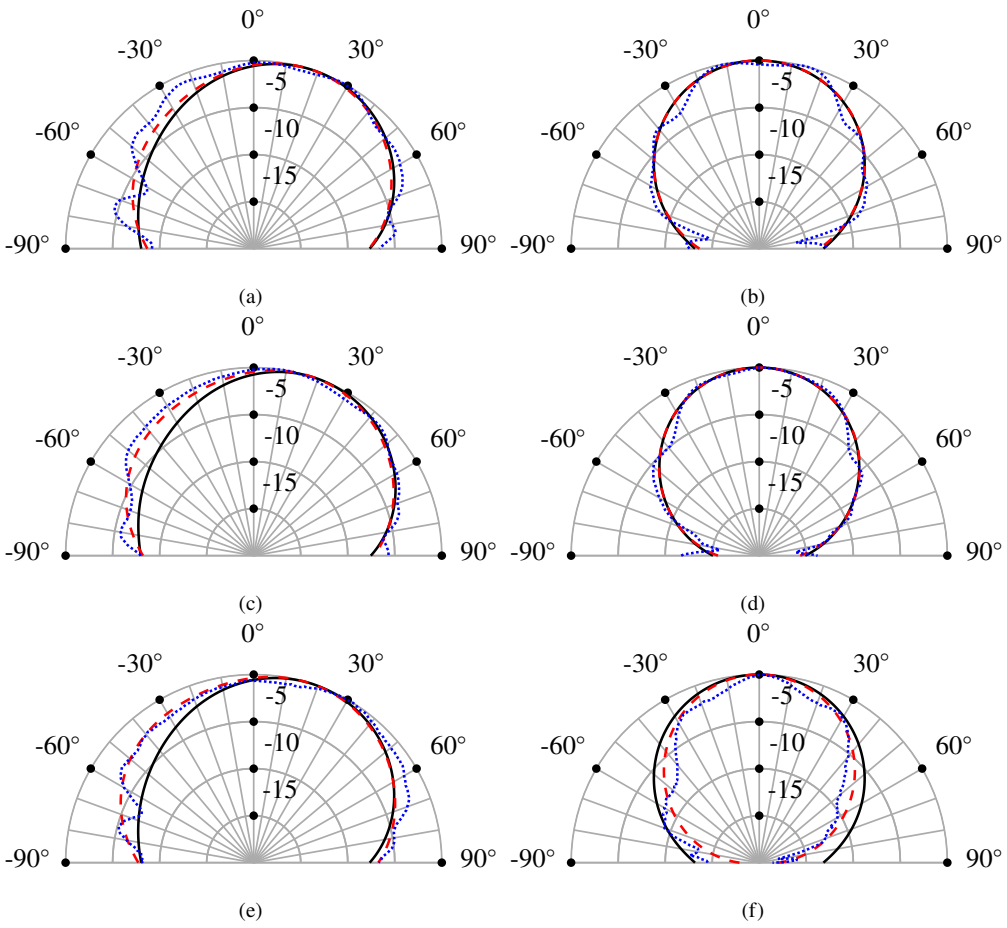

Fig. 7. Normalized free-space far-field gain patterns [dB] of the half-mode air-filled substrate-integrated-waveguide antenna (simulated —) and the transmit remote antenna unit (simulated - - - and measured · · ·) at the lower frequency 5.15 GHz (top row), center frequency 5.50 GHz (middle row), and at the upper frequency 5.85 GHz (bottom row), both in the E-plane (left column), and the H-plane (right column).

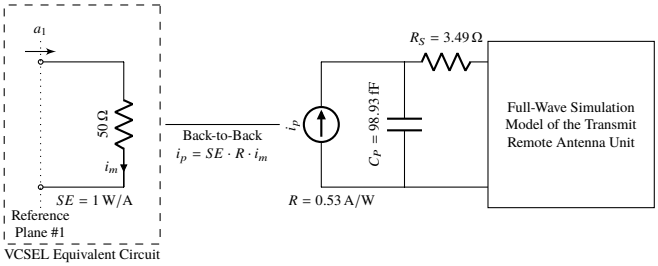

Fig. 8. Full-wave simulation model for the far-field boresight gain of the full transmit remote antenna unit.

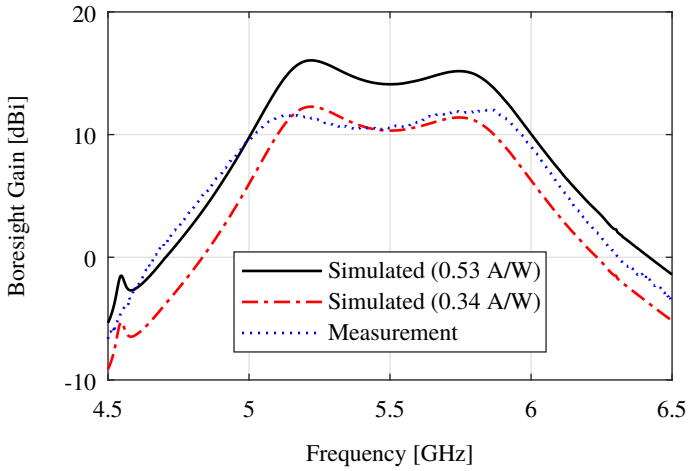

Fig. 9. Normalized far-field boresight gain [dBi] of the transmit remote antenna unit (simulation, excluding and including fiber-pigtail coupling efficiency, and measurement), as a function of frequency.

over an ultra-wide bandwidth of 840 MHz or 15.3 %). The simulated normalized far-field gain patterns in the E- and H-planes, at the lower, center, and upper frequency, are shown by the red dashed lines in Fig. 7.

By applying the proposed conjugate-impedance matching procedure, the amount of RF power extracted from the photodetector and, thereby, the transmit RAU's far-field gain is increased significantly. This is proven by Fig. 10, which compares the simulated transducer gain (defined as the fraction of the maximum power available from the photodetector that is actually delivered to the antenna) of the proposed conjugate-matched design to the nominal case where the photodetector is directly interconnected to a 50 Ω antenna. In the nominal case, a very low transducer gain is obtained in the frequency band of interest (on average 0.8 %), as a result of the large impedance mismatch. By contrast, a much higher transducer gain is obtained in case of the proposed conjugate-matched design (on average 19.2 %), which is specifically enhanced in the frequency band of interest.

3. Validation and measurements

A prototype of the optimized transmit RAU is deployed inside the anechoic chamber, as shown in Fig. 11. It is experimentally validated by measuring the free-space radiation pattern at several

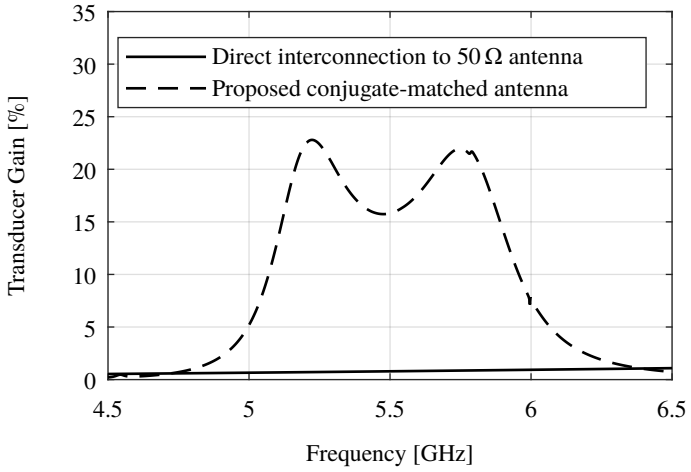

Fig. 10. Simulated transducer gain [%] (defined as the fraction of the maximum power available from the photodetector that is actually delivered to the antenna) as a function of frequency in case the photodetector is directly interconnected to a 50 Ω antenna (solid line), and in case of the proposed conjugate-matched design (dashed line).

frequencies. The employed measurement setup is shown schematically in Fig. 12. The first port of a VNA, located in a shielded room, directly modulates an 850 nm optical source. The reference plane for the radiation pattern measurement is located at the modulation input of the optical source, as indicated in Fig. 12. Specifically, a 12.5 Gbps VCSEL by Finisar (HFE6192-761) is employed as the optical source, which is biased by a current of 6 mA, resulting in an average optical output power of −3.33 dBm. The slope efficiency of the employed VCSEL is characterized in the frequency band of interest by means of an Optilab PD-40-MM-M photodetector, resulting in an average value of 0.043 W/A. This is somewhat reduced compared to the nominal value listed in the VCSEL's datasheet, as a result of additional losses and parasitics occurring in the connectorized PCB assembling the VCSEL. While such a low slope efficiency is detrimental to the gain of the analog optical link [35], this VCSEL is only used for validation and not considered part of the transmit RAU. Therefore, all subsequent measurements are normalized with respect to the measured slope efficiency of the VCSEL. To evaluate the photodetector's responsivity, the VCSEL is first directly connected to the transmit RAU. A photocurrent of 0.159 mA is observed, indicating a fiber-coupled responsivity of $0.34\,\mathrm{A\,W^{-1}}$. As the nominal responsivity amounts to $0.53\,\mathrm{A\,W^{-1}}$, the fiber pigtail achieves a high coupling efficiency of 64 %. Subsequently, the VCSEL is attached to a 10-meter long multimode fiber, which is routed inside the anechoic chamber and connected to the 2-meter long multimode pigtail of the transmit RAU prototype. The VNA's second port is connected to a standard gain horn (MI-12-3.9 or MI-12-5.8), located in the far-field of the transmit RAU, in order to evaluate its far-field gain pattern through the gain comparison method.

Initially, the boresight gain bandwidth of the prototype was too low and shifted towards lower frequencies, such that the frequency band of interest was not covered. This is attributed to a higher amount of index-matching epoxy that is deposited around the photodetector's bonding wires than foreseen during design. Nevertheless, by completely shorting the GCPW stub by means of copper tape, operation in the correct frequency band could still be obtained. The resulting boresight gain as a function of frequency is depicted by the blue dotted curve in Fig. 9. This measurement is normalized with respect to the measured slope efficiency of the VCSEL,

in order to enable comparison to the simulation, which is shown by the red dash-dotted curve in Fig. 9 and employs an ideal optical source, with an input impedance of 50 Ω and a slope efficiency of 1 W A^{-1}. Despite the necessary tuning, a good agreement between simulation and measurement is observed. A maximum normalized boresight gain of 12.0 dBi and a −3 dB gain bandwidth of 1020 MHz (18.6 %), which ranges from 4.98 GHz to 6.00 GHz, are measured, covering the frequency band of interest. Furthermore, the measured far-field gain patterns, normalized with respect to the maximum value, are shown in Fig. 7 by the blue dotted lines, for the E- and H-planes at multiple frequencies, being the lower frequency of 5.15 GHz, the center frequency of 5.50 GHz, and the upper frequency of 5.85 GHz. While a good agreement between simulation and measurement is observed in the H-plane, the measured E-plane beam width is considerably wider as compared to the simulation. This discrepancy is attributed to the antenna measurement fixture, shown in Fig. 11. As the E-plane coincides with the vertical plane in Fig. 11, the measurement fixture affects the E-plane radiation pattern more than the radiation pattern in the H-plane. In Table 2, measurements of several important far-field performance metrics are summarized and compared to the simulated values, again at the lower, center, and upper frequency. These include the normalized boresight gain, the boresight cross-polarization level and the 3 dB beam widths in the E- and H-planes, which are defined as the angle between the points on the main lobe where the gain has decreased by 3 dB with respect to the maximum value.

Furthermore, Table 2 lists the equivalent isotropic radiated power (EIRP) that was transmitted by the prototype when the optical source was excited by an RF power of 0 dBm. The relatively low EIRP realized by the prototype is caused by the extremely low slope efficiency of the employed VCSEL (HFE6192-761), which significantly degrades the gain of the analog optical link [17]. When a more suitable optical source is employed, such as a V50-850M multi-mode VCSEL by Vertically Integrated Systems with a nominal slope efficiency of 0.375 W A^{-1}, higher EIRP values over 0 dBm are obtainable.

Finally, it is verified that dispersion-induced power fading [36] resulting from the multi-mode fiber does not severely impact the performance of the prototype. As the proposed transmit RAU is intended for application in the novel communication system proposed in [3], where the RAUs are embedded in a factory floor, the fiber length is expected to remain relatively short, up to a few hundred meters. In Fig. 13, the measured normalized boresight gain is presented for several fiber lengths up to 512 m, indicating that the gain slightly decreases with increasing fiber length. This does not only result from the losses in the additional fiber segments, but also from the increased connector losses. As a result, the proposed transmit RAU is validated for use with multi-mode fiber with a length up to 512 m and a directly modulated VCSEL at the considered RF frequencies.

Table 2. Measured (simulated) far-field radiation properties and equivalent isotropic radiated power (EIRP) of the transmit remote antenna unit at several frequencies.

Characteristic	5.15 GHz	5.50 GHz	5.85 GHz
Boresight Gain [dBi]	11.6 (11.5)	10.5 (10.3)	12.0 (10.4)
Cross-polarization level [dB]	−35.2 (−59.1)	−31.0 (−56.6)	−20.0 (−53.6)
E-plane beam width [°]	116 (90)	117 (102)	127 (112)
H-plane beam width [°]	58 (72)	62 (68)	63 (64)
EIRP (HFE6192-761) [dBm]	−17.4	−18.3	−17.1
EIRP (V50-850M) [dBm]	(1.8)	(0.5)	(1.9)

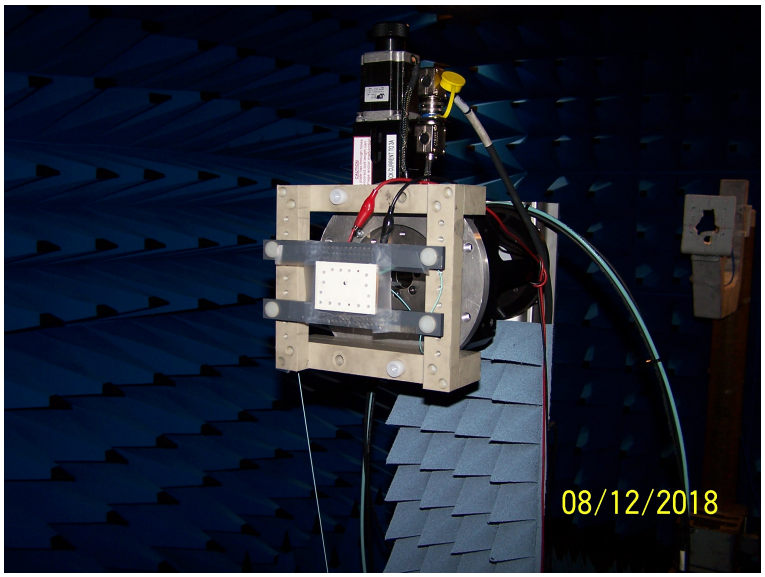

Fig. 11. Prototype of the proposed transmit remote opto-antenna unit deployed in the anechoic chamber.

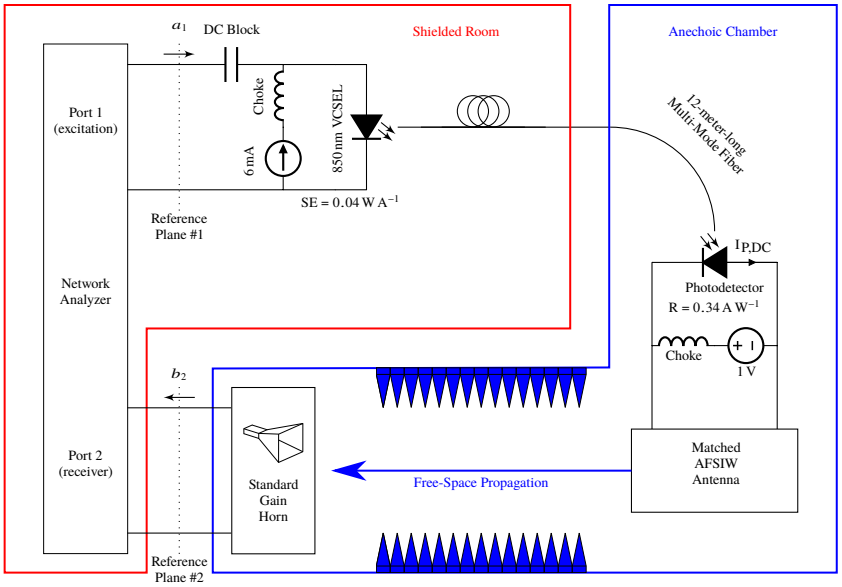

Fig. 12. Measurement setup for the far-field radiation pattern of the transmit remote antenna unit prototype.

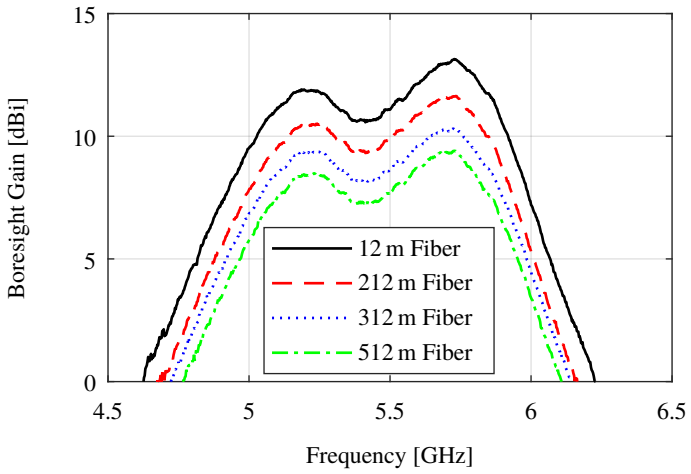

Fig. 13. Normalized far-field boresight gain [dBi] of the transmit remote antenna unit as a function of frequency, measured for several fiber lengths.

4. Conclusion and outlook

We have proposed a novel transmit RAU, that achieves conjugate matching between a photodetector and a high performance half-mode air-filled substrate-integrated-waveguide antenna. As electrical amplifiers were omitted, the unit only requires an externally supplied bias voltage for the photodetector and is, therefore, nearly passive. When deployed in an analog optical link, the radiated power is extracted entirely from the optical signal supplied by a multi-mode fiber. A novel co-design strategy was described, in which the photodetector is almost directly connected to the antenna, which is designed as a conjugate-matched load, such that the radiated power is optimized in a specified bandwidth. A novel half-mode air-filled substrate-integrated-waveguide antenna topology was proposed, which is able to realize the required input impedance. With respect to previous designs, this novel approach avoids the use of area-consuming distributed elements, leading to a more compact design with fewer losses and less spurious radiation. Owing to its cost effectiveness, power efficiency and robustness, the unit is ideally suited for massive deployment in innovative wireless communication systems, featuring extremely dense attocells of 15 cm $\times$ 15 cm.

As a next step, the proposed transmit RAU should be extended towards mm-wave frequencies. The resulting compact mm-wave transmit RAU would be particularly suitable for deployment in large antenna arrays, since optical beam forming networks [37–40] could be employed. These offer compelling advantages over full electrical array feeding networks, including smaller size, lower weight, immunity to electromagnetic interference, and squint-free beam steering of broadband signals by exploiting optical true-time delay units. To scale the design towards mm-wave frequencies, a limited number of adjustments are required, in particular replacing the chip inductor by a more viable alternative, such as a microstrip spiral inductor, and adopting another antenna feeding mechanism, such as aperture coupling. Furthermore, the power of multiple photodetectors could be combined to increase the transmit power of the unit. When absolutely necessary, the use of amplifiers could be reconsidered to increase transmit power. Finally, the functionality of the proposed transmit RAU could be significantly extended by applying metalenses to generate vortex beams carrying orbital angular momentum [41] or meta-deflectors [42].

Acknowledgments

The authors would like to thank the ERC for the advanced grant 695495 “ATTO: A new concept for ultra-high capacity wireless networks”. The authors would also like to thank Ing. Jan Gillis of the Department of Information Technology, Ghent University, and Dr. Björn Vandecasteele and Prof. Jeroen Missinne of the Centre for Microsystems Technology (CMST) at Ghent University, for their skillful help and advice during assembly of the prototypes.

References

1. C. Lim, A. Nirmalathas, M. Bakaul, P. Gamage, K. L. Lee, Y. Yang, D. Novak, and R. Waterhouse, “Fiber-wireless networks and subsystem technologies,” J. Light. Technol. **28**, 390–405 (2010).
2. D. Novak, R. B. Waterhouse, A. Nirmalathas, C. Lim, P. A. Gamage, T. R. Clark, M. L. Dennis, and J. A. Nanzer, “Radio-over-fiber technologies for emerging wireless systems,” IEEE J. Quantum Electron. **52**, 1–11 (2016).
3. G. Torfs, H. Li, S. Agneessens, J. Bauwelinck, L. Breyne, O. Caytan, W. Joseph, S. Lemey, H. Rogier, A. Thielens, D. Vande Ginste, J. Van Kerrebrouck, G. Vermeeren, X. Yin, and P. Demeester, “ATTO: Wireless networking at fiber speed,” J. Light. Technol. **36**, 1468–1477 (2018).
4. B. Lannoo, A. Dixit, D. Colle, J. Bauwelinck, B. Dhoedt, B. Jooris, I. Moerman, M. Pickavet, H. Rogier, P. Simoens, G. Torfs, D. Vande Ginste, and P. Demeester, “Radio-over-fibre for ultra-small 5G cells,” in *2015 17th International Conference on Transparent Optical Networks (ICTON),* (2015), pp. 1–4.
5. Federal Communications Commission, “Revision of Part 15 of the Commission’s Rules to Permit Unlicensed National Information Infrastructure (U-NII) Devices in the 5 GHz Band, ET Docket No. 13-49,” released February 20, 2013.
6. D. Wake, N. G. Walker, and I. C. Smith, “Zero-bias edge-coupled InGaAs photodiodes in millimetre-wave radio-fibre systems,” Electron. Lett. **29**, 1879–1881 (1993).
7. N. Chen, H. Tsai, F. Kuo, and J. Shi, “High-speed w-band integrated photonic transmitter for radio-over-fiber applications,” IEEE Transactions on Microw. Theory Tech. **59**, 978–986 (2011).
8. K. Takahata, Y. Muramoto, S. Fukushima, T. Furuta, and H. Ito, “Monolithically integrated millimeter-wave photonic emitter for 60-GHz fiber-radio applications,” in *International Topical Meeting on Microwave Photonics MWP 2000 (Cat. No.00EX430),* (2000), pp. 229–232.
9. K. Li, X. Xie, Q. Li, Y. Shen, M. E. Woodsen, Z. Yang, A. Beling, and J. C. Campbell, “High-power photodiode integrated with coplanar patch antenna for 60-GHz applications,” IEEE Photonics Technol. Lett. **27**, 650–653 (2015).
10. N. Shimizu and T. Nagatsuma, “Photodiode-integrated microstrip antenna array for subterahertz radiation,” IEEE Photonics Technol. Lett. **18**, 743–745 (2006).
11. A. Hirata, H. Ishii, and T. Nagatsuma, “Design and characterization of a 120-GHz millimeter-wave antenna for integrated photonic transmitters,” IEEE Transactions on Microw. Theory Tech. **49**, 2157–2162 (2001).
12. A. Stohr, S. Babiel, P. J. Cannard, B. Charbonnier, F. van Dijk, S. Fedderwitz, D. Moodie, L. Pavlovic, L. Ponnampalam, C. C. Renaud, D. Rogers, V. Rymanov, A. Seeds, A. G. Steffan, A. Umbach, and M. Weiss, “Millimeter-wave photonic components for broadband wireless systems,” IEEE Transactions on Microw. Theory Tech. **58**, 3071–3082 (2010).
13. S. Shi, J. Bai, R. Nelson, C. Schuetz, P. Yao, G. J. Schneider, Y. Zhang, and D. W. Prather, “Ultrawideband optically fed tightly coupled phased array,” J. Light. Technol. **33**, 4781–4790 (2015).
14. M. R. Konkol, D. D. Ross, S. Shi, C. E. Harrity, A. A. Wright, C. A. Schuetz, and D. W. Prather, “Photonic tightly coupled array,” IEEE Transactions on Microw. Theory Tech. **66**, 2570–2578 (2018).
15. M. R. Konkol, D. D. Ross, S. Shi, C. E. Harrity, A. A. Wright, C. A. Schuetz, and D. W. Prather, “High-power photodiode-integrated-connected array antenna,” J. Light. Technol. **35**, 2010–2016 (2017).
16. D. D. Ross, M. R. Konkol, S. Shi, C. E. Harrity, A. A. Wright, C. A. Schuetz, and D. W. Prather, “Low-profile high-power optically addressed phased array antenna,” J. Light. Technol. **35**, 3894–3900 (2017).
17. C. H. Cox, E. I. Ackerman, G. E. Betts, and J. L. Prince, “Limits on the performance of RF-over-fiber links and their impact on device design,” IEEE Transactions on Microw. Theory Tech. **54**, 906–920 (2006).
18. H. Bode, *Network Analysis and Feedback Amplifier Design*, Bell Telephone Laboratories series (Van Nostrand, 1945).
19. R. Fano, “Theoretical limitations on the broadband matching of arbitrary impedances,” J. Frankl. Inst. **249**, 57 – 83 (1950).
20. O. Caytan, L. Bogaert, H. Li, J. Van Kerrebrouck, S. Lemey, G. Torfs, J. Bauwelinck, P. Demeester, S. Agneessens, D. Vande Ginste, and H. Rogier, “Passive opto-antenna as downlink remote antenna unit for radio frequency over fiber,” J. Light. Technol. **36**, 4445–4459 (2018).
21. A. Belenguer, H. Esteban, and V. E. Boria, “Novel empty substrate integrated waveguide for high-performance microwave integrated circuits,” IEEE Transactions on Microw. Theory Tech. **62**, 832–839 (2014).
22. Q. Van den Brande, S. Lemey, J. Vanfleteren, and H. Rogier, “Highly-efficient impulse-radio ultra-wideband cavity-backed slot antenna in stacked air-filled substrate-integrated-waveguide technology,” IEEE Transactions on Antennas Propag. **66**, 2199–2209 (2018).
23. J. V. Morro, A. Rodríguez, A. Belenguer, H. Esteban, and V. Boria, “Multilevel transition in empty substrate integrated waveguide,” Electron. Lett. **52**, 1543–1544 (2016).
24. M. E. Godinez, C. S. McDermitt, A. S. Hastings, M. G. Parent, and F. Bucholtz, “RF characterization of zero-biased photodiodes,” J. Light. Technol. **26**, 3829–3834 (2008).

25. D. Wake, A. Nkansah, N. J. Gomes, C. Lethien, C. Sion, and J. P. Vilcot, "Optically powered remote units for radio-over-fiber systems," J. Light. Technol. **26**, 2484–2491 (2008).
26. L. Breyne, G. Torfs, X. Yin, P. Demeester, and J. Bauwelinck, "Comparison between analog radio-over-fiber and sigma delta modulated radio-over-fiber," IEEE Photonics Technol. Lett. **29**, 1808–1811 (2017).
27. C. L. Goldsmith and B. Kanack, "Broadband microwave matching of high speed photodiodes," in *1993 IEEE MTT-S International Microwave Symposium Digest,* (1993), pp. 233–236 vol.1.
28. D. Pozar, *Microwave Engineering* (Wiley, 2004).
29. G. Matthaei, L. Young, and E. Jones, *Microwave filters, impedance-matching networks, and coupling structures*, Artech House Microwave Library (McGraw-Hill, 1964).
30. R. Levy, "Explicit formulas for chebyshev impedance-matching networks, filters and interstages," Proc. Inst. Electr. Eng. **111**, 1099–1106 (1964).
31. C. Jin, R. Li, A. Alphones, and X. Bao, "Quarter-mode substrate integrated waveguide and its application to antennas design," IEEE Transactions on Antennas Propag. **61**, 2921–2928 (2013).
32. T. Deckmyn, S. Agneessens, A. C. F. Reniers, A. B. Smolders, M. Cauwe, D. Vande Ginste, and H. Rogier, "A novel 60 GHz wideband coupled half-mode/quarter-mode substrate integrated waveguide antenna," IEEE Transactions on Antennas Propag. **65**, 6915–6926 (2017).
33. G. A. E. Vandenbosch and A. R. Van de Capelle, "Study of the capacitively fed microstrip antenna element," IEEE Transactions on Antennas Propag. **42**, 1648–1652 (1994).
34. H. F. Pues and A. R. Van de Capelle, "An impedance-matching technique for increasing the bandwidth of microstrip antennas," IEEE Transactions on Antennas Propag. **37**, 1345–1354 (1989).
35. C. H. Cox, E. I. Ackerman, G. E. Betts, and J. L. Prince, "Limits on the performance of RF-over-fiber links and their impact on device design," IEEE Transactions on Microw. Theory Tech. **54**, 906–920 (2006).
36. U. Gliese, S. Norskov, and T. N. Nielsen, "Chromatic dispersion in fiber-optic microwave and millimeter-wave links," IEEE Transactions on Microw. Theory Tech. **44**, 1716–1724 (1996).
37. W. Ng, A. A. Walston, G. L. Tangonan, J. J. Lee, I. L. Newberg, and N. Bernstein, "The first demonstration of an optically steered microwave phased array antenna using true-time-delay," J. Light. Technol. **9**, 1124–1131 (1991).
38. M. Y. Frankel, P. J. Matthews, and R. D. Esman, "Fiber-optic true time steering of an ultrawide-band receive array," IEEE Transactions on Microw. Theory Tech. **45**, 1522–1526 (1997).
39. B. Vidal, T. Mengual, C. Ibanez-Lopez, and J. Marti, "Optical beamforming network based on fiber-optical delay lines and spatial light modulators for large antenna arrays," IEEE Photonics Technol. Lett. **18**, 2590–2592 (2006).
40. B. Jung, J. Shin, and B. Kim, "Optical true time-delay for two-dimensional x-band phased array antennas," IEEE Photonics Technol. Lett. **19**, 877–879 (2007).
41. K. Zhang, Y. Yuan, D. Zhang, X. Ding, B. Ratni, S. N. Burokur, M. Lu, K. Tang, and Q. Wu, "Phase-engineered metalenses to generate converging and non-diffractive vortex beam carrying orbital angular momentum in microwave region," Opt. Express **26**, 1351–1360 (2018).
42. Y. Yuan, K. Zhang, X. Ding, B. Ratni, S. N. Burokur, and Q. Wu, "Complementary transmissive ultra-thin meta-deflectors for broadband polarization-independent refractions in the microwave region," Photonics Res. **7**, 80–88 (2019).